ELSEVIER

Contents lists available at ScienceDirect

Journal of Alloys and Compounds

journal homepage: http://www.elsevier.com/locate/jalcom



Evolution of microstructure and hardness in Hf₂₅Nb₂₅Ti₂₅Zr₂₅ high-entropy alloy during high-pressure torsion



Jenő Gubicza ^{a, *}, Anita Heczel ^a, Megumi Kawasaki ^b, Jae-Kyung Han ^b, Yakai Zhao ^c, Yunfei Xue ^c, Shuo Huang ^d, János L. Lábár ^{a, e}

- ^a Department of Materials Physics, Eötvös Loránd University, Budapest, P.O.B. 32, H-1518, Hungary
- ^b School of Mechanical, Industrial and Manufacturing Engineering, Oregon State University, Corvallis, OR 97331, USA
- ^c School of Materials Science and Engineering, Beijing Institute of Technology, Beijing 100081, China
- d Applied Materials Physics, Department of Materials Science and Engineering, Royal Institute of Technology, 100 44 Stockholm, Sweden
- e Institute for Technical Physics and Materials Science, Centre for Energy Research, Hungarian Academy of Sciences, Budapest, Hungary

ARTICLE INFO

Article history: Received 17 December 2018 Received in revised form 3 February 2019 Accepted 18 February 2019 Available online 21 February 2019

Keywords:
High-entropy alloys
Severe plastic deformation
Nanostructured materials
Microstructure
Dislocations
Hardness

ABSTRACT

A four-component equimolar high-entropy alloy (HEA) with the composition of HfNbTiZr and body-centered cubic (bcc) structure was processed by HPT at RT. The evolution of the dislocation density, the grain size and the hardness was monitored along the HPT-processed disk radius for different numbers of turns between ½ and 20. It was found that most of the increase of the dislocation density and the refinement of the grain structure occurred up to the shear strain of ~40. Between the strains of ~40 and ~700, only a slight grain size reduction was observed. The saturated dislocation density and grain size were ~2.1 \times 10¹⁶ m⁻² and ~30 nm, respectively. The saturation in hardness was obtained at ~4450 MPa. These values were similar to the parameters determined in the literature for five-component HEAs processed by HPT. The analysis confirmed that the main component in the strength was given by the friction stress in the HPT-processed bcc HfNbTiZr HEA. It was also revealed that the contribution of the high dislocation density to the strength was significantly higher than the effect of the small grain size.

© 2019 Elsevier B.V. All rights reserved.

1. Introduction

High-entropy alloys (HEAs) are generally defined as alloys with more than five major elements in equal or near equal atomic percentage, in contrast to conventional alloys which consist of only one or two major elements [1,2]. Recently, a significant research attention has been paid to HEAs due to their outstanding properties, such as high hardness and strength, good resistance to thermal softening, oxidation, wear, and corrosion [1–6]. It was revealed that, although the number of major constituents was reduced to four or three, the properties of alloys (e.g., the hardness) did not become worse whereas the stability of the disordered solid solution decreased due to the lower entropy [7]. The materials with three major elements are referred to as medium entropy alloys (MEAs) while the samples containing four constituents with equal fractions are called as either HEAs or MEAs in the literature [8–11].

It is well known that the mechanical properties of metallic materials can be tailored by severe plastic deformation (SPD). During SPD, the lattice defect density (such as the dislocation density and the vacancy concentration) increases while the grain sizes are strongly reduced. As a result, the strength of the SPDprocessed materials is considerably enhanced. The most effective SPD method in grain refinement refers to high-pressure torsion (HPT). In alloys, HPT usually results in a nanocrystalline microstructure, which may yield a microhardness as high as 6000 MPa [12]. Therefore, in order to improve the strength of HEAs HPT has been applied on these materials [7–28]. It was found that HPT at room temperature (RT) can reduce the grain size from hundreds of microns to tens of nanometers [13,17,19,22,24,25]. In addition, the dislocation density increased to a very high value of about 10^{16} m⁻² [17,18]. In face-centered cubic (fcc) HEAs with low stacking fault energy (SFE), nanotwins are additionally formed in the nanograins during HPT, thereby contributing to the high strength of HEAs [7,15–17]. It was found that these changes in the microstructure (the increase of the dislocation and twin fault densities, and the decrease of the grain size) enhanced the hardness from about 1500

^{*} Corresponding author.

E-mail address: jeno.gubicza@ttk.elte.hu (J. Gubicza).

to 2000 MPa to 4000–6000 MPa in both fcc and body-centered cubic (bcc) HEAs [17,18,21,22].

A majority of the HEA materials processed by HPT have fcc structure and only a few studies investigated bcc structure [26,27]. In these papers, an equimolar HfNbTiZrTa HEA with bcc structure was processed by HPT at RT and the deformed microstructure and its thermal stability were studied in details. Another investigation found that if the fractions of Nb and Ta were reduced in HfNbTiZrTa HEA to the composition of Ti₃₅Zr_{27.5}Hf_{27.5}Nb₅Ta₅, the initial coarsegrained bcc material transformed into an orthorhombic ultrafinegrained (UFG) structure during HPT [18]. Therefore, it is worth investigating the HEA composition of HfNbTiZr where Ta is perfectly absent. Wu et al. [29] studied the structural stability, the deformation and the fracture features of a coarse-grained HfNbTiZr HEA. This HEA exhibited excellent phase stability at high temperatures and no phase separation occurred during furnace cooling from the homogenization temperature of 1573 K. In the as-cast state, the yield strength was 879 MPa, the ultimate tensile strength was 969 MPa, and the plastic elongation to failure was 14.9%. However, to the knowledge of the authors the study of the microstructure and the mechanical properties of equimolar HfNbTiZr HEA processed by HPT is missing in the literature.

Accordingly, this paper was initiated to investigate the evolution of the microstructure and the hardness during HPT-processing of a bcc HfNbTiZr HEA. The grain size and the dislocation density were determined by transmission electron microscopy (TEM) and X-ray line profile analysis (XLPA), respectively. The comprehensive investigation evaluated the relationship between dislocation density, grain size and hardness of the nanocrystalline HfNbTiZr HEA.

2. Material and methods

2.1. Processing of the material

 $Hf_{25}Nb_{25}Ti_{25}Zr_{25}$ HEA samples were synthesized by magnetic levitation melting of a mixture of the four pure components (purity > 99.9 wt%), followed by solid solution heat treatment at 1290 °C for 24 h. The as-cast material was machined into billets with a diameter of 10 mm and these were sliced by electric discharge machining (EDM) to have a final thickness of ~0.85 mm. Processing by HPT was conducted by utilizing a conventional HPT facility with quasi-constrained set-up [30]. The processing was operated at room temperature under 6.0 GPa at 1 rpm for the numbers of turns of $\frac{1}{2}$, 1, 10 and 20.

2.2. Study of the microstructure by electron microscopy

The grain structure was studied in the initial as-cast sample, as well as in the centers and the peripheries of the HPT-processed disks where the applied strain values were the lowest and highest, respectively. In the centers of the disks processed by 1/4 and 1 turn, it was feasible to investigate the grain structure by electron backscatter diffraction (EBSD). Since at the peripheries of the HPT samples and in the centers of the disks processed by 10 and 20 turns the grain size was too small to examine by EBSD, transmission electron microscopy (TEM) was used for the study of the microstructure. The EBSD was carried out using an FEI Quanta 3D scanning electron microscope (SEM). The investigated area was prepared by ion milling for 20 min using an Ar ion beam with an energy of 10 keV and an angle of incidence of ~5°, followed by surface cleaning with an energy of 1 keV for 5 min and an angle of incidence of ~7°. The surface preparation was carried out by a SEMPrep (SC-1000) device from Technoorg Linda. During ion milling of the surface, the samples were cooled using liquid nitrogen in order to avoid the recovery and/or recrystallization of the SPD-processed microstructure. The step size in the EBSD images varied between $8\,\mu m$ and $60\,nm$, depending on the magnification. The higher magnification required a smaller step size. The EBSD images were evaluated using the Orientation Imaging Microscopy (OIM) software.

For the TEM characterization, thin TEM-lamellae were prepared from pieces of bulk samples by Ar-ion milling with taking special care to avoid heating leading to microstructural changes and possible transformation of the samples during preparation. First, the samples were glued to a Cu-stub for mechanical grinding and polishing using special glue at 100 °C for not more than 1 min. Second, ion-beam thinning of the 50 µm thick lamella was started at 7 keV using 2 mA ion-current. The samples were cooled with liquid nitrogen during thinning. Finally, the just perforated lamella was cleaned at 3 keV and later at 1 keV from both sides to remove damaged layers from its surfaces. TEM bright-field (BF) and darkfield (DF) images were recorded in a Titan Themis G2 200 transmission electron microscope. In this device, the corrector for the spherical aberration (C_s) is in the imaging part. The image resolution limit is 0.09 nm in phase-contrast HRTEM mode. The TEM images were recorded at 200 keV with a 4k*4k CETA 16 CMOS camera controlled by VELOX software. The number of grains analyzed in the TEM images for each sample was between 90 and 120. The uncertainty of the average grain size values was about 10%.

2.3. Microstructure characterization by X-ray diffraction

The phase composition in the initial and the HPT-processed HEA samples was investigated by X-ray diffraction (XRD) using a Rigaku Smartlab powder diffractometer with CuK α radiation (wavelength: $\lambda = 0.15418$ nm). All studied materials had a single phase bcc structure. The average lattice parameter was determined by extrapolating the lattice parameters obtained from the different reflections to the diffraction angle of $2\Theta = 180^\circ$ using the Nelson–Riley method [31].

The microstructure in the center and the peripheral parts of the HPT-processed disks was studied by XLPA. The X-ray line profiles were measured by a high-resolution rotating anode diffractometer (type: RA-MultiMax9, manufacturer: Rigaku) using CuKα₁ (wavelength: $\lambda = 0.15406 \text{ nm}$) radiation. Two-dimensional imaging plates were used to detect the Debye-Scherrer diffraction rings. The line profiles were determined as the intensity distribution perpendicular to the rings. The diffraction profiles were evaluated by the Convolutional Multiple Whole Profile (CMWP) method [32]. In this method, the diffraction pattern is fitted by the sum of a background spline and the convolution of the instrumental pattern and the theoretical line profiles related to diffraction domain size and dislocations. The instrumental diffraction peaks were measured on a LaB₆ standard material (SRM 660). Reflection 222 was omitted from the pattern due to its weak intensity. The CMWP method gave the area-weighted mean diffraction domain size $(\langle x \rangle_{area})$, the dislocation density (ρ) and parameter q which describes the edge/screw character of dislocations with good statistics. The value of $\langle x \rangle_{\text{area}}$ is calculated as $\langle x \rangle_{\text{area}} = m \cdot \exp(2.5 \sigma^2)$, where m is the median and σ^2 is the log-normal variance of the diffraction domain size distribution [9]. It is noted that the height of the X-ray beam spot on the sample surface was about 2 mm. Therefore, the results obtained in the disk center should be considered as an average for distances from the center smaller than 1 mm, as shown in Fig. 1. At the periphery, the XLPA measurement was carried out at 1 mm from the edge and therefore at a distance of 4 mm from the disk center (see Fig. 1).

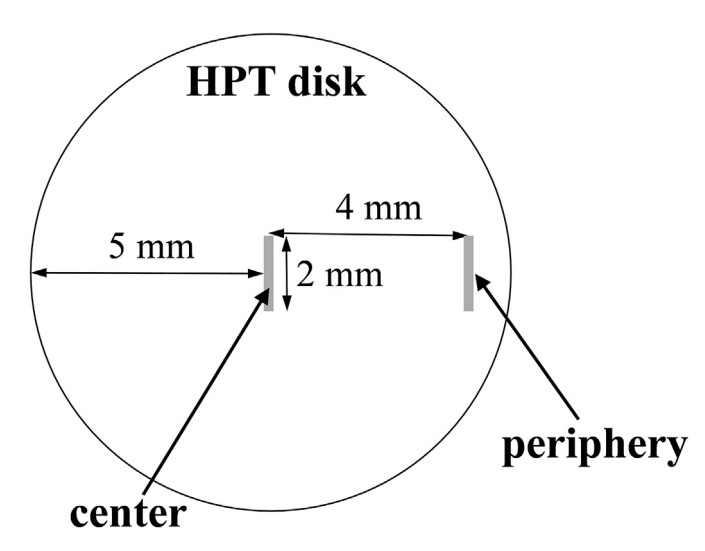


Fig. 1. Schematic showing the position and the size of the XRD beam used for XLPA measurements at the center and the periphery of HPT disks.

2.4. Hardness testing

The hardness was measured along the disk diameter with a step size of 0.5 mm. The hardness test was carried out using a Zwick Roell ZH μ Vickers indenter with an applied load of 500 g and a dwell time of 10 s.

3. Results

3.1. Evolution of grain size during HPT-processing

The XRD investigation revealed that the initial material before HPT had a bcc structure with a lattice constant of 0.3438 ± 0.0003 nm. The HPT-processed samples remained a single phase bcc structure with an unchanged lattice parameter. Fig. 2a and b show crystallographic orientation and grain maps, respectively, for the initial sample as obtained by EBSD. The grains were defined as the volumes bounded by high-angle grain boundaries (HAGBs) with the misorientations of higher than 15°. The average grain size obtained from the grain map was ~640 μ m. Fig. 3a and b display the crystallographic orientation and grain maps, respectively, at the center of the disk processed by ¼ turn of HPT. The upper-left corner of these images corresponds to the center of the disk where large grains with the size of several hundreds of micrometers are still visible. On the other hand, about 1 mm apart from the center of the disk the grain size was smaller than the step

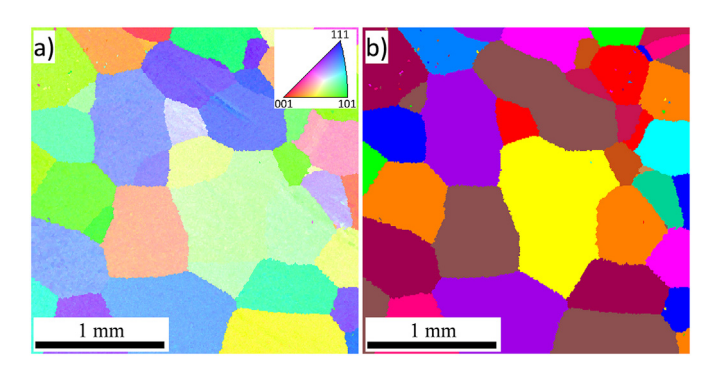


Fig. 2. Crystallographic orientation (a) and grain (b) maps obtained on the initial sample by EBSD.

size in the EBDS images (6 µm), due to the strong increase of the shear strain with increasing the distance from the center. In these areas, the color in the orientation map changes from pixel to pixel, and the grain map is white. Therefore, a part of Fig. 3a was taken again with a smaller step size of 800 nm and this orientation map is shown in Fig. 3c, and the corresponding grain map is displayed in Fig. 3d. It can be seen that the finer step size used in Fig. 3c and d helped to reveal the small grains in the area denoted by the black frame in Fig. 3a and b. However, Fig. 3c and d also contain unresolved parts which can be mapped with a lower step size (60 nm) in Fig. 3e (orientation map) and Fig. 3f (grain map). The average grain size in Fig. 3e was determined as ~270 nm. Assuming that this value is characteristic for the unresolved white regions in Fig. 3b, the average grain size in the vicinity of the center was calculated as the average of this value and the mean size of the large resolved grains in Fig. 3b (~33 µm) weighted with the area fractions of the white and colored areas in Fig. 3b (these fractions were ~58% and ~41% for the white and colored areas, respectively). Thus, an average grain size of ~13 µm was obtained for the center part of the disk processed by 1/4 turn.

The consistent tendency of the grain size gradient was also observed in the center of the sample processed by 1 turn as shown in the EBSD orientation and grain maps taken with a step size of 2 μm in Fig. 4a and b, respectively. In this case, the center of the disk can be found in the middle of the left edge of the images where the grain size is still a several hundreds of micrometers. Smaller grains can also been seen in Fig. 4c and d taken with a step size of 400 nm. However, about 0.5 mm apart from the center the grain structure became unresolved with the EBSD images as indicated by the white areas in Fig. 4d, therefore TEM was used to determine the grain size in these volumes. Fig. 5a and b show BF and DF TEM images taken at a distance of 0.5 mm from the disk center after 1 turn of HPT. The grain size was obtained from DF images as $64 \pm 10 \, \text{nm}$ and this value was considered as the characteristic grain size in the white regions in Fig. 4b. Then, the mean grain size for the center part shown in Fig. 4b was calculated as the weighted average of the grain sizes obtained for the colored and white regions by EBSD and TEM, respectively. In this calculation, the weights were the area fractions of the colored and white regions in Fig. 4b with the values of \sim 68% and \sim 32%, respectively. The estimated grain size was \sim 5 μm for the center of the disk processed by 1 turn of HPT. Regarding the determination of the grain size by TEM, it should be noted that the grains are elongated in the center of the disk processed by 1 turn (see Fig. 5b). Therefore, the grain size was estimated as the average of the longer and shorter diagonals of ~100 grains for each sample. Moreover, the light areas in the DF images were taken as grains whereas these areas contain bright spots which were considered as subgrains. In the vicinity of the center of the disk processed by 1 turn, the subgrain size was determined as 27 ± 4 nm. For all studied samples, both the grain and subgrain sizes are listed in Table 1. For the center parts of the disks processed by ¼ and 1 turn, the subgrain size is not given in Table 1 as the larger grains shown in the EBSD images were not included in the TEM investigations, therefore the subgrain sizes obtained by TEM do not characterize the whole center parts. It is worth noting that the disk centers processed by 1/4 and 1 turn include lamellas developed inside the large grains as shown at the right side of Fig. 3e and in the upper part of Fig. 4c, respectively. The boundaries of these lamellas were identified as Σ 19a and Σ 19b boundaries which correspond to the misorientation angles of 26.5° and 46.8°, respectively.

For 10 and 20 turns, the grain sizes at the disk centers were very small (40–50 nm) and the TEM analysis was sufficient for the size determination. Fig. 5c—f show TEM images taken in the centers of the disks processed by 10 and 20 turns. The average grain and subgrain sizes obtained from these images are listed in Table 1.

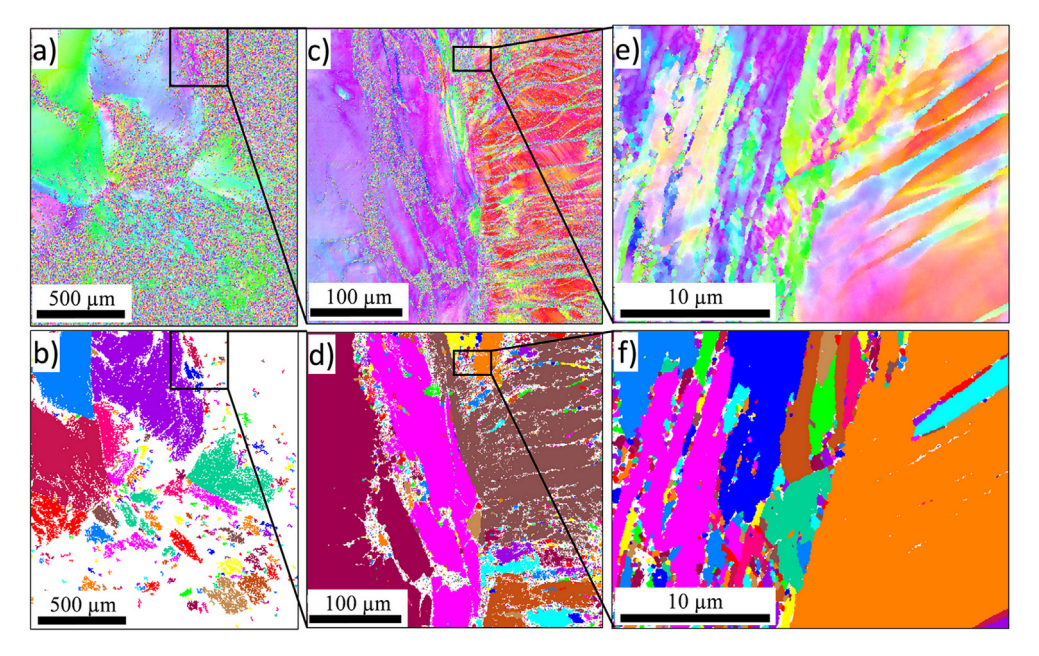


Fig. 3. Crystallographic orientation (a) and grain (b) maps taken at the center of the disk processed by ¼ turn of HPT. The upper-right corner of these images corresponds to the center of the disk. The area indicated by the frame in (a) and (b) was taken again with a smaller step size and shown in (c) and (d), respectively. Furthermore, the framed area in (c) and (d) was taken again with a smaller step size and shown in (e) and (f), respectively.

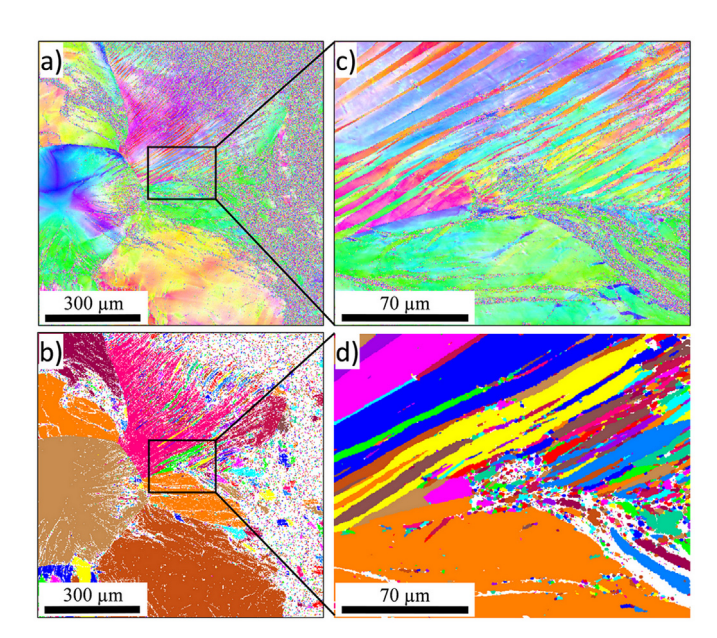


Fig. 4. Crystallographic orientation (a) and grain (b) maps taken at the center of the disk processed by 1 turn of HPT. The middle of the left edge of these images corresponds to the center of the disk. The area indicated by the frame in (a) and (b) was taken again with a smaller step size and shown in (c) and (d), respectively.

After HPT for 10 and 20 turns, the average grain sizes in the centers were 48 ± 7 nm and 42 ± 6 nm, respectively and the subgrain size was ~15 nm for both samples. Fig. 6 shows TEM images obtained at the peripheries at ~4 mm away from the disk centers after $\frac{1}{4}$, 1, 10 and 20 turns. The grain sizes determined at the peripheral parts are listed in Table 1. After $\frac{1}{4}$ turn, the grain size was about 100 nm which decreased to ~30 nm for 10 turns, and this value remained unchanged between 10 and 20 turns of HPT. The subgrain size was 35 ± 5 nm at the periphery after $\frac{1}{4}$ turn. This value decreased to ~16 nm after 1 turn and further subgrain size reduction was not

observed with increasing the number of turns. It should be emphasized that twin faults were not observed by TEM in the nanocrystalline HfNbTiZr HEA processed by HPT at RT.

3.2. Characterization of the microstructure by XLPA

XLPA on the HPT-processed HEA samples was carried out using the CMWP fitting procedure. In the CMWP evaluation method, one fitting parameter is $\overline{C}_{h00}b^2\rho$, where *b* is the modulus of the Burgers vector of dislocations and \overline{C}_{h00} is the dislocation contrast factor for reflections with the indices h00 (h is an arbitrary integer number). The Burgers vector for bcc crystal structures is given as a/2 < 111 > $\{110\}$, where a is the lattice constant, thus b equals 0.2977 nm for the present HEA material. Since \overline{C}_{h00} depends on the anisotropic elastic constants, without the knowledge of their values the dislocation density cannot be determined. Using the ab initio alloy theory presented in Ref. [33], the single crystal elastic constants were calculated. The values of the elastic constants c_{11} , c_{12} , and c_{44} for the studied HEA at 300 K were obtained as 132, 89, and 77 GPa, respectively, where this is the first report computing the elastic constants for the Hf₂₅Nb₂₅Ti₂₅Zr₂₅ HEA. Using the program ANIZC (http://metal.elte.hu/anizc), the two parameters of the dislocation contrast factors, \overline{C}_{h00} and q were determined for pure screw and pure edge dislocations. The calculations demonstrated the values of q for pure edge and pure screw dislocations of 1.5 and 2.7, respectively. In the CMWP fitting procedure for the determination of the diffraction domain size and the dislocation density, the average values of \overline{C}_{h00} obtained for pure edge and pure screw cases (0.31) was used since \overline{C}_{h00} are almost independent on the edge/ screw character of dislocations.

The CMWP fitting is illustrated in Fig. 7 where the measured and the fitted XRD patterns are shown for the center of the disk processed by 20 turns. It is noted that in HEAs the chemical inhomogeneities may also cause diffraction peak broadening in addition to the instrumental, size and lattice defect contributions, as shown for CoCrFeMnNi HEA in Ref. [17]. On the contrary, energy

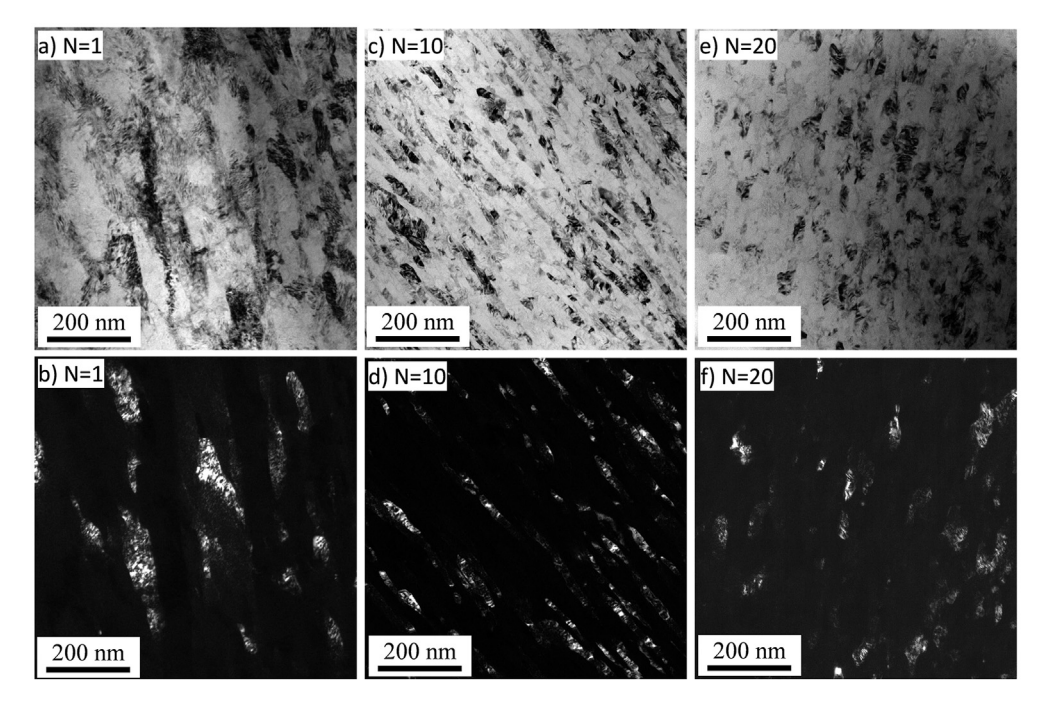
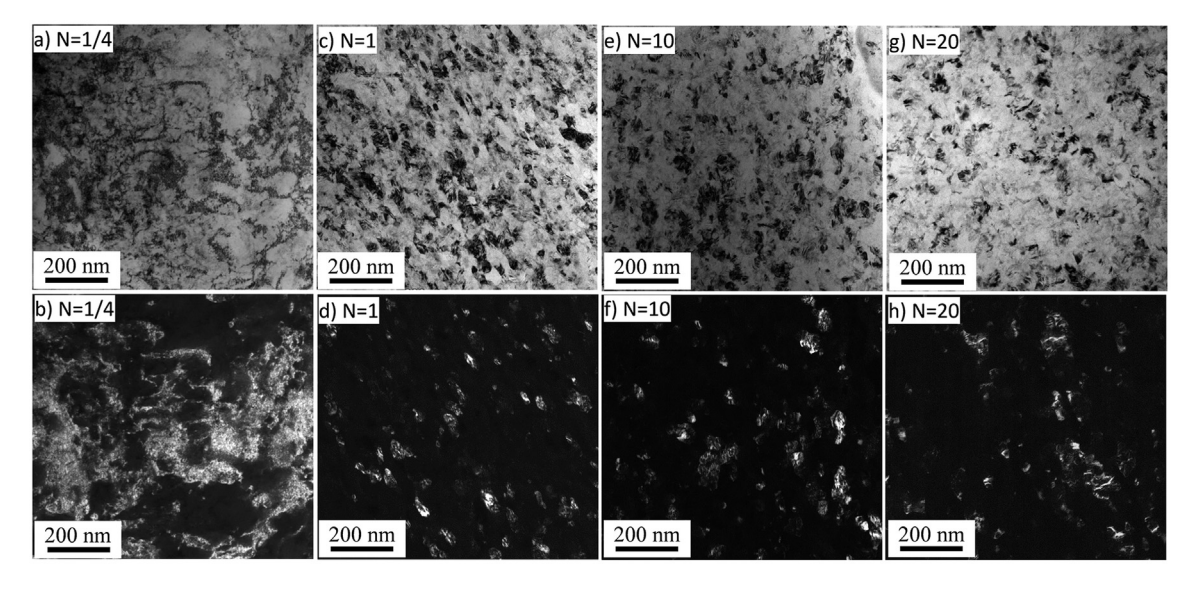


Fig. 5. BF and DF TEM images taken at a distance of 0.5 mm from the disk center after 1 (a,b), 10 (c,d) and 20 (e,f) turns of HPT.

Table 1The dislocation density and the diffraction domain size determined by XLPA, as well as the grain and subgrain sizes obtained by electron microscopy (EBSD and TEM).

Location	Dislocation density (XLPA) $[10^{14}\text{m}^{-2}]$	Diffraction domain size (XLPA) [nm]	Subgrain size (TEM) [nm]	Grain size (EBSD/TEM) [nm]
1/4, center	39 ± 4	124 ± 19	n.a.	~13,000
1/4, periphery	138 ± 15	31 ± 5	35 ± 5	105 ± 15
1, center	146 ± 16	54 ± 8	n.a.	~7000
1, periphery	208 ± 23	18 ± 3	16 ± 2	41 ± 6
10, center	207 ± 23	17 ± 3	15 ± 2	48 ± 7
10, periphery	210 ± 23	18 ± 3	16 ± 2	31 ± 5
20, center	211 ± 23	18 ± 3	14 ± 2	42 ± 6
20, periphery	214 ± 24	17 ± 3	13 ± 2	28 ± 4



 $\textbf{Fig. 6.} \ \ \textbf{BF} \ \ \textbf{and} \ \ \textbf{DF} \ \ \textbf{TEM} \ \ \textbf{images} \ \ \textbf{taken} \ \ \textbf{at} \ \ \textbf{a} \ \ \textbf{distance} \ \ \textbf{of} \ \ \textbf{1} \ \ \textbf{mm} \ \ \textbf{from} \ \ \textbf{the} \ \ \textbf{disk} \ \ \textbf{periphery} \ \ \textbf{after} \ \ \ \ \ \ \ \textbf{4} \ \ (\textbf{c,d}), \ \ \textbf{10} \ \ (\textbf{e,f}) \ \ \textbf{and} \ \ \textbf{20} \ \ (\textbf{g,h}) \ \ \textbf{turns} \ \ \textbf{of} \ \ \textbf{HPT}.$

dispersive spectroscopy (EDS) did not reveal considerable chemical heterogeneities for the present HEA, and the breadth of the peak

profiles obtained for the initial as-cast sample was the same as the instrumental broadening measured on LaB₆ standard material.

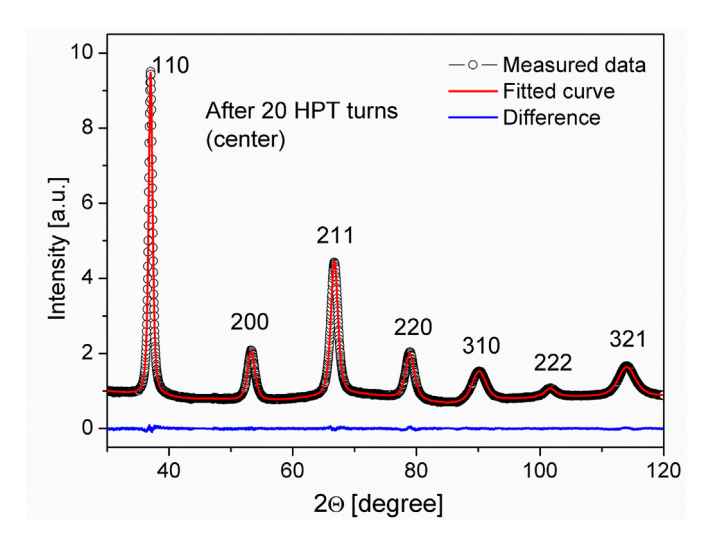


Fig. 7. CMWP evaluation of the XRD pattern obtained at the center of the disk processed by 20 turns of HPT. The open circles and the solid line represent the measured and fitted diffractograms, respectively. The difference between these two patterns is shown at the bottom of the figure.

Therefore, the correction introduced for chemically inhomogeneous materials in Ref. [17] was not applied here.

The dislocation density and the diffraction domain size values obtained by CMWP at the centers and the peripheries of the HPTprocessed disks are listed in Table 1. The diffraction domain size was 124 + 19 nm in the disk center after 1/4 turn of HPT. This value is much smaller than the grain size determined by the combination of EBSD and TEM (~13 μm, see Table 1). This is a well known phenomenon in the SPD-processed UFG materials as the small misorientations between the subgrains inside the grains lead to incoherent scattering of X-rays. Therefore, the diffraction domain size usually corresponds to the subgrain size. This is also valid in the present HEA samples for the locations where subgrain sizes were measurable by TEM (see Table 1). The diffraction domain size decreased to 31 ± 5 nm at the periphery of the disk processed by $\frac{1}{4}$ turn. After 1 turn, there is still a gradient in the diffraction domain size along the disk radius as its value is 54 ± 8 nm in the center and 18 ± 3 nm at the periphery. At the same time, for 10 and 20 turns the diffraction domain size is 17–18 nm at both the center and the periphery of the disks. Therefore, this value can be regarded as the saturation diffraction domain size achievable by HPT at RT in the Hf₂₅Nb₂₅Ti₂₅Zr₂₅ HEA. This value also characterizes the minimum subgrain size while the saturation grain size is about 30 nm.

The dislocation density was $(39\pm4)\times10^{14}\,\mathrm{m}^{-2}$ in the center of the disk processed for ½ turn. This value increased to $(138\pm15)\times10^{14}\,\mathrm{m}^{-2}$ at the periphery of this sample. After 1 turn of HPT, the dislocation density increased to $\sim\!146\times10^{14}\,\mathrm{m}^{-2}$ and $\sim\!210\times10^{14}\,\mathrm{m}^{-2}$ in the center and the periphery, respectively. The latter value is the saturation dislocation density which was achieved in both the centers and the peripheries after both 10 and 20 turns of HPT (see Table 1).

3.3. Hardness evolution in the HPT-processed disks

The hardness variation as a function of the distance from the disk center is plotted in Fig. 8 for the disks after ¼, 1, 10 and 20 turns where the dashed horizontal line indicates the hardness of the initial sample before HPT (~2630 MPa). After ¼ turn of HPT, only a negligible increase in the hardness was observed in the center (~2690 MPa) and with a gradual hardness increase with distance from the disk center its value increased to ~3570 MPa at the

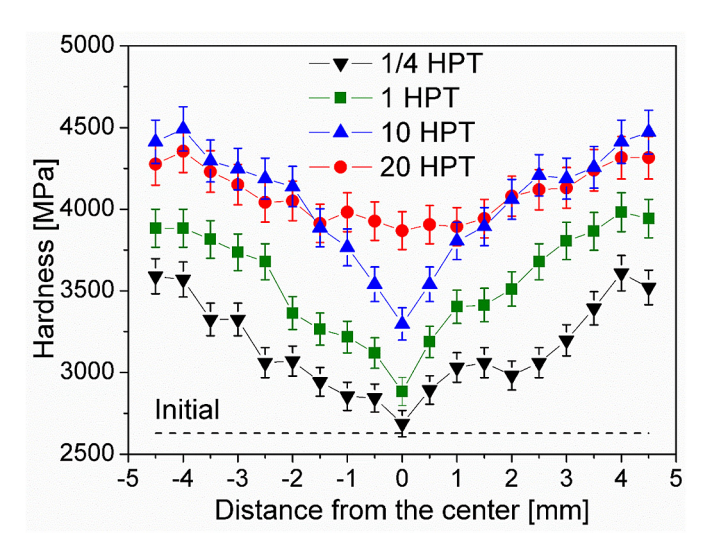


Fig. 8. Vickers microhardness as a function of the distance from the center of the disks processed by HPT for ¼, 1, 10 and 20 turns. The dashed line shows the average hardness in the initial as-cast condition without HPT.

periphery of the disk. One turn resulted in a considerable enhancement in hardness across the disk diameter where the disk center records ~2880 MPa and the periphery showed ~3920 MPa. After 10 turns, a further increase in hardness was demonstrated so that the values reached to ~3300 and ~4450 MPa at the center and the periphery, respectively. 20 turns by HPT increased the hardness at the disk center to ~3870 MPa so that the hardness difference across the disk diameter became smaller where the periphery shows ~4330 MPa that can be regarded as the saturated maximum hardness in the Hf₂₅Nb₂₅Ti₂₅Zr₂₅ HEA processed by HPT at RT.

4. Discussion

4.1. Evolution of microstructure and hardness with increasing shear strain imposed during HPT

The evolution of the dislocation density and the diffraction domain size determined by XLPA, and the grain size obtained by electron microscopy as a function of shear strain is plotted in Fig. 8. The shear strain was determined by the following formula [34]:

$$\gamma = \frac{2\pi rN}{t},\tag{1}$$

where r. N and t are the distance from the disk center, the number of turns and the thickness of the disk, respectively. It should be noted that eq. (1) gives only the nominal shear strain in the HPTprocessed disk. In practice, before the starting of the torsional deformation the samples were loaded under 6.0 GPa, resulting in a preliminary compression strain of about 20%. In addition, although eq. (1) gives zero strain in the center of the disks, the actual strain is not zero since the stress field of dislocations developed out of the disk center induces dislocation motion in the center [35]. Therefore, the plasticity spreads into the center from the neighboring regions during HPT-processing. Although, anvil misalignment may also cause strain in the disk center, this effect was negligible in the present study since all samples were processed under the wellmaintained and consistent anvil set-up. It should also be noted that as the height of the X-ray spot on the illuminated surface is 2 mm, the value of γ in the center was calculated by averaging the strain values obtained for the distances from the disk center between zero and 1 mm (see Fig. 1). This is equivalent to the strain obtained for r = 0.5 mm using eq. (1). The grain size was also averaged around this location as discussed in section 3.1. At the periphery, the microstructure was investigated by both XLPA and TEM at a distance of 4 mm from the disk center (see Fig. 1), thereby the shear strain was also calculated at r = 4 mm using eq. (1).

Fig. 9a shows that the dislocation density increased monotonously with increasing shear strain and then saturated with the value of $\sim\!\!210\times10^{14}\,\mathrm{m}^{-2}$ at a strain of $\sim\!\!40$. Afterwards, the dislocation density remained constant between the shear strains of $\sim\!\!40$ and $\sim\!\!700$. A similar trend was observed for the crystallite size for which the saturation value was $\sim\!\!17$ nm (see Fig. 9b). In the same way, most of the grain refinement was completed up to the strain of $\sim\!\!40$ while the saturation in the grain size was achieved only after the shear strain of $\sim\!\!400$ as shown in Fig. 9c where the grain size was plotted in a logarithmic scale since its value changed orders of magnitude in the studied strain range.

The evolution of the hardness as a function of the shear strain is shown in Fig. 9d where this plot contains all the points shown in Fig. 8. It reveals that the hardness values measured at different distances from the disk centers for various numbers of turns follow a unified trend when they are plotted as a function of the shear strain. A very fast hardening was observed up to the strain of ~40 which was caused by both the increase of the dislocation density (see Fig. 9a) and the reduction of the grain size (see Fig. 9c), and these are followed by a moderate hardness enhancement up to the strain of 400. Since the dislocation density saturated at the strain of ~40 and deformation twins were not observed in the TEM images. the increase of the hardness above this strain can be attributed to the further grain refinement from 40 to 50 nm-~30 nm. The relationship between the hardness and the microstructural parameters will be discussed in section 4.3. Similar hardness evolution was observed for conventional pure metals and alloys, such as Fe [36], austenitic steel [37], Al-7075 [38], AZ80 [39] and interstitial-free steel [40], as well as for other HEAs, such as CoCrFeNiMn and CoCrFeNiMnTi_{0.1} [19], i.e., most of the hardness increment occurred up to the shear strain of ~40 and for higher strains only a moderate strengthening or a saturation of the hardness was observed.

4.2. Comparison of the microstructure and hardness obtained for the HPT-processed $Hf_{25}Nb_{25}Ti_{25}Zr_{25}$ alloy with other HEAs

It is worth to compare the saturation microstructural parameters and hardness obtained for the present $Hf_{25}Nb_{25}Ti_{25}Zr_{25}$ alloy with the values determined for other HEAs processed by HPT at RT. Table 2 shows the saturation hardness, dislocation density and grain size obtained for the HEAs deformed by HPT at RT. Only the values of dislocation density were shown in the table where those were determined by the reliable X-ray full pattern fitting methods. Moreover, Table 2 shows the grain size obtained by TEM which is often different from the diffraction domain size determined by XLPA. In order to avoid the indentation size effect [41], only the microhardness values are summarized in the table.

Table 2 shows that the majority of the HPT-processed HEAs studied in the literature have single phase fcc or bcc structure with a saturation grain size between 30 and 100 nm and hardness in the range of 4000-6000 MPa. Exceptionally high hardness with the value of 6520 MPa was measured on an AlNbTiVZr_{0.5} HEA consisting of 86% B2 phase and 14% C14 Laves phase [23]. This multiphase microstructure and the very small grain size (25 nm) could cause the significantly high hardness of this sample. For most single phase HEAs shown in Table 2, the achievable minimum grain size and the maximum hardness were about 30 nm and 5000 MPa. respectively, although very different compositions and structures were studied. Indeed, if we compare the present bcc HfNbTiZr HEA with these fcc HEAs, such as CoCrFeMnNi, Al_{0.3}CoCrFeNi and CoCrFeNiMnTi_{0.1}, the minimum grain size is consistent for all of these structures as about 30 nm (see Table 2). The saturation microhardness values of these fcc HEAs are between 4510 and 5380 MPa which are slightly higher than for the present bcc HfNbTiZr HEA of 4450 ± 110 MPa. The difference in the hardness may be attributed to the different dislocation densities in the different structures. Thus, it is reasonable to compare the

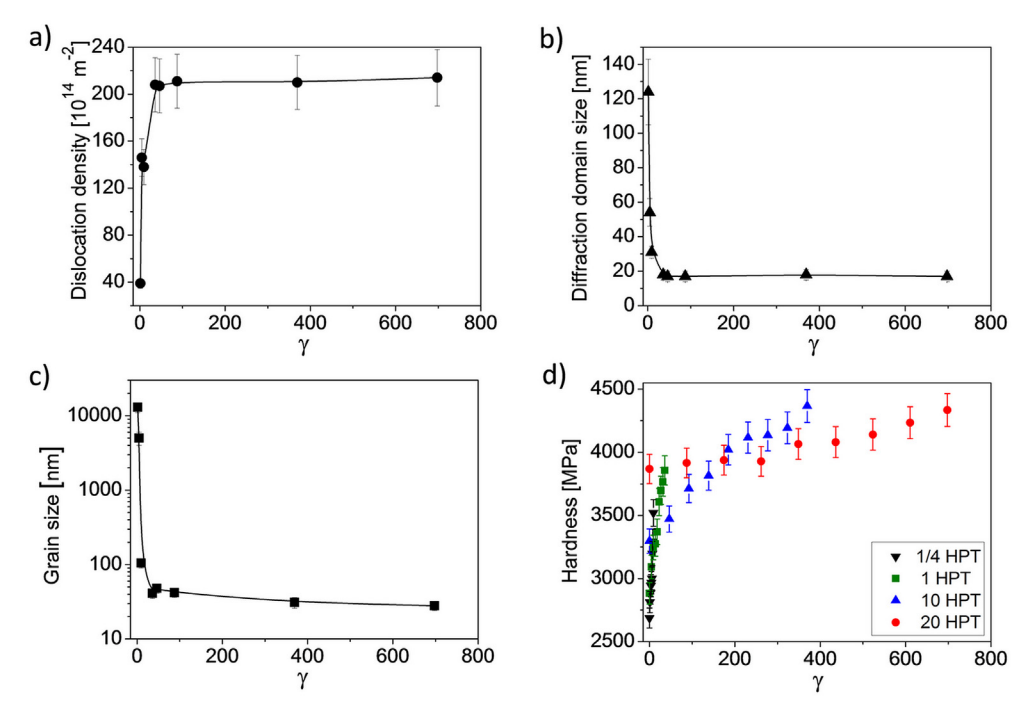


Fig. 9. The evolution of the dislocation density (a) and the diffraction domain size (b) obtained by XLPA, as well as the grain size determined by TEM (c) and the microhardness (d) as a function of the nominal shear strain calculated from eq. (1).

Table 2
The saturation dislocation density determined by XLPA, the grain size obtained by TEM and the hardness determined for different HEAs and MEAs processed by HPT at RT. The crystallographic structure of the different HEAs is indicated in the parentheses after the compositions. In addition to the grain size, the twin boundary (TB) spacing is also shown for some fcc HEAs with low stacking fault energy.

Composition	Dislocation density [10 ¹⁴ m ⁻²]	Grain size (TB spacing) [nm]	Hardness [MPa]	Reference
HfNbTiZr (bcc)	211 ± 23	28 ± 4	4450 ± 110	This study
HfNbTaTiZr (bcc)	_	80	5000 ± 400	[26]
HfNbTaTiZr (bcc)	_	50	4120 ± 20	[27]
Ti ₃₅ Zr _{27.5} Hf _{27.5} Nb ₅ Ta ₅ (orthorhombic)	100 ± 10	600	3900 ± 100	[18]
CoCrFeMnNi (fcc)	194 ± 20	$27 \pm 5 (8)$	5380 ± 120	[17]
FeCoCrNi (fcc)	_	70 (20)	5200	[16]
CoCrNi (fcc)	_	50 (5)	5980	[7]
$Co_{20}Cr_{26}Fe_{20}Mn_{20}Ni_{14}$ (fcc)	_	61 ± 25	5500 ± 200	[21]
Al _{0.1} CoCrFeNi (fcc)	_	80 (7)	4730	[15]
Al _{0.3} CoCrFeNi (fcc)	_	30	5200	[13,24]
CoCrFeNiMnTi _{0.1} (fcc)	_	30	4510	[19,22,25]
FeNiCoCu (fcc)	_	100	3430	[14]
(FeNiCoCu) ₈₆ Ti ₇ Al ₇ (fcc)	_	50	5150	[14]
Al _{0.5} CoCrFeMnNi (82% fcc + 18% B2 phase)	_	_	5200 ± 200	[20]
$AlNbTiVZr_{0.5} \ (86\% \ B2 \ phase + 14\% \ C14 \ Laves \ phase)$	_	25	6520	[23]

dislocation density between the present bcc HEA and the reported fcc CoCrFeMnNi [17]. The saturation dislocation density was obtained as about $200 \times 10^{14} \, \text{m}^{-2}$ for fcc CoCrFeMnNi HEA which is practically the same as that for the present bcc HfNbTiZr HEA. Despite the very similar grain size and dislocation density, the hardness of the fcc CoCrFeMnNi HEA ($5380 \pm 120 \text{ MPa}$) is larger than that for the present bcc HfNbTiZr HEA (4450 \pm 110 MPa). The higher hardness for the fcc HEA can be attributed to the large twin fault density formed during HPT processing due to the low SFE of this alloy. In the saturation state, the average twin boundary spacing inside the nanograins was ~8 nm [17]. These twin faults hinder the dislocation motion in a similar way as grain boundaries, thereby leading to the hardening in the fcc CoCrFeMnNi HEA. A fcc CoCrNi MEA processed by HPT with the twin boundary spacing of only ~5 nm [7] yielded even higher hardness (5980 MPa) than that for a CoCrFeMnNi HEA (5380 MPa) despite the larger grain size of the former alloy (~50 nm).

The microstructure and hardness of the present HPT-processed HfNbTiZr HEA are worth to be compared with the features of a counterpart containing Ta, i.e., with HfNbTaTiZr processed by HPT at RT [26,27]. Both compositions form a bcc structure and a similar saturation hardness (4000–5000 MPa) as shown in Table 2. As the values of the threshold stress of plasticity (i.e., the friction stress) are very close for HfNbTiZr [29] and HfNbTaTiZr [42] HEAs (about 880 MPa), the similar hardness suggests similar microstructural strengthening in the saturation state obtained by HPT at RT.

4.3. Relationship between microstructure and hardness

For revealing the strengthening contributions of the grain boundaries and dislocations in the HPT-processed HfNbTiZr HEA, these two hardening effects were calculated from the measured dislocation densities and the grain sizes, and their sum was compared with the total yield strength where the value was estimated as one-third of the measured hardness [43]. It should be noted that one-third of the microhardness corresponds to the flow stress at a plastic strain of 8% [43]. In general, SPD-processed metallic materials exhibit low strain hardening, thus the yield strength and the flow stress at a plastic strain of 8% can be considered reasonably consistent. It should also be noted that former HRTEM studies [7,16] revealed many dislocations inside the grains in HPT-processed HEAs even for grain sizes smaller than 100 nm. Therefore, the interaction between dislocations emitted from grain boundaries and dislocations stored inside the grains contributes to the hardness, which can be taken into account by a Taylor term.

The strengthening contribution of dislocations can be obtained from the Taylor equation as [44]:

$$\sigma_{Taylor} = \alpha M^T G b \sqrt{\rho}, \tag{2}$$

where α is a constant describing the strengthening effect of dislocations, G is the average shear modulus (~46 GPa for HfNbTiZr HEA as determined from the elastic constants, see section 3.2), b is the modulus of the Burgers vector (0.2977 nm for the present HEA) and M^T is the Taylor factor (3.06 was selected as a strong texture was not observed). The grain size strengthening can be described by the Hall–Petch formula [45,46]:

$$\sigma_{HP} = \frac{k}{\sqrt{d}},\tag{3}$$

where k is a material constant and d is the grain size. Assuming a linear additivity of the hardening contributions of dislocations and grain size, the total yield strength can be obtained as:

$$\sigma_{y} = \sigma_{0} + \sigma_{Taylor} + \sigma_{HP}, \tag{4}$$

where σ_0 is the friction stress. The value of σ_0 was taken as ~879 MPa in accordance with a former study which determined σ_0 from tension of a coarse-grained HfNbTiZr HEA with a similar grain size as for the present HEA [29]. In the Taylor and Hall-Petch equations, α and k are unknown parameters. In this analysis, the values of these parameters were determined by searching for the best agreement between the estimated yield strength (obtained as one-third of the hardness) and the values calculated from eq. (4) for the centers and the peripheries of the disks. As mentioned earlier at Fig. 1, the hardness values used in the analysis are the average values at the selected measurement regions.

The best achievable agreement between the yield strength calculated from eq. (4) and the estimated strength determined from the hardness is shown in Fig. 10. It can be seen that the datum points are in the vicinity of the solid line representing a perfect agreement between the calculated and estimated values. The corresponding values of α and k are 0.05 ± 0.01 and 29 ± 3 MPa μ m $^{1/2}$, respectively. Using these values in eqs. (2) and (3), the contributions of dislocations and grain size to the yield strength were calculated and listed in Table 3. A large contribution of friction stress is evident with 90% at lower HPT turns up to 60% at higher HPT turns to the total strength. This is much higher than that of fcc

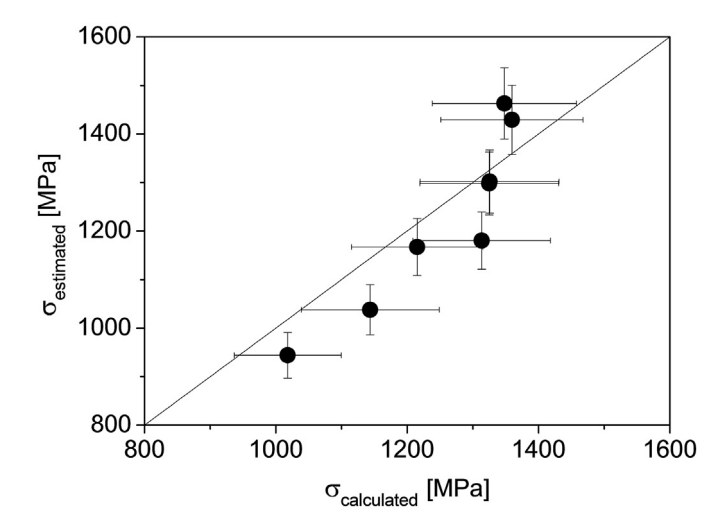


Fig. 10. The estimated yield strength versus the values calculated from eq. (4) for the center and the periphery of the disks processed by $\frac{1}{4}$, 1, 10 and 20 turns.

HEAs processed by HPT. For instance, this value was only 10-20% for HPT-processed CoCrFeMnNi HEA [17]. This difference can be explained by the reduced mobility of dislocations in bcc structures which is caused at least partially by the dissociation of screw dislocation cores into a non-planar configuration. In fcc crystals, dislocations are split into partials only in their glide planes which does not hinder their slip.

Former studies have shown that the classical Hall-Petch relation remained valid until the grain size decreased below a critical value which was about 10-20 nm for the different metallic materials. For smaller grain sizes, an inverse Hall-Petch behavior was observed. For instance, for bcc-Fe the critical grain size of the inverse Hall-Petch behavior was ~15 nm [50]. Although significant grain refinement was achieved in different types of HEAs by HPT, to our best knowledge, the grain size was not reduced below 20 nm. Therefore, the occurrence of an inverse Hall-Petch behavior is not expected in HPT-processed HEAs. At the same time, the Hall-Petch slope (k) may vary slightly with decreasing grain size to the nanocrystalline regime as shown for some conventional materials such as Cu [51]. This deviation from the conventional Hall-Petch behavior can be attributed to the grain size dependence of the stress required to operate dislocation sources. This effect, however, should result in a reduction of the value of k with decreasing grain size which would yield a downward deflection of the points plotted for high strength values in Fig. 10. At the same time, rather there is an upward deviation from the straight line obtained with a constant Hall-Petch slope at high strength which may be caused by an increased value of k. Indeed, a former study [40] has shown that a higher grain boundary misorientation can result in a larger Hall-Petch slope in HPT-processed bcc metallic materials. Thus, an increase of grain boundary misorientation for high HPT strains might have caused a larger grain boundary strengthening, leading to a slightly higher measured strength than the value calculated with the assumption of an unchanged Hall-Petch slope.

It should be noted that α is very small (~0.05) compared to the values received formerly for other bcc materials (0.16-0.60 [42,47–49]). The clarification of this effect requires further studies. The values of α and k in eqs. (2) and (3) may vary with increasing strain during HPT [51], and the single values of these parameters obtained from the present evaluation are only approximations for α and k. Nevertheless, the grain boundary strengthening tends to be essential for the strength of the present HEA as the hardening above the shear strains of ~40 can only be explained by the change of the grain size strengthening. It should be noted, however, that the Hall-Petch slope obtained for the present HPT-processed bcc HfNbTiZr HEA samples is smaller than the values available in the literature for other HEAs processed by HPT [52–54]. The difference can be attributed to fact that in other studies the contributions of lattice defects (such as dislocations and twin faults) to strength were not considered in the evaluation of hardening caused by HPT. Indeed, when the strengthening contributions of dislocations and twin faults were taken into account in the analysis of the hardness of a HPT-processed CoCrFeMnNi HEA, a similar value of k was obtained as in the present study [17]. It is also evident from Table 3 that the dislocation strengthening is higher at least with a factor of two than the strength contribution caused by the grain size. Therefore, it concludes the excellent feasibility of HPT for strengthening the HEA by grain refinement and dislocation multiplication.

5. Conclusions

The evolution of microstructure and hardness during HPT-processing of a bcc HfNbTiZr HEA was studied. The following conclusions were obtained:

- 1. The saturation dislocation density was about $2.1 \times 10^{16} \, \mathrm{m}^{-2}$ which was achieved after the shear strain of ~40 while further increase in shear through ~700 did not introduce any significant change. Most grain refinement occurred below the shear strain of ~40 where the average grain size decreased from ~640 μ m to 40–50 nm while a minimum grain size of ~30 nm was observed in further straining to ~400. At low strains, lamellas with Σ 19a and Σ 19b boundaries were formed inside the grains. The saturation dislocation density and grain size in the HfNbTiZr HEA were similar to the values reported for five-component HEAs.
- 2. Corresponding to the grain refinement and increased dislocation density, significant hardness enhancement took place from

Table 3
The contributions of dislocations (σ_{Taylor}) and grain size (σ_{HP}) to the yield strength calculated from the Taylor and Hall-Petch relationships according to eqs. (2) and (3), respectively, and the value of the friction stress (σ_0). The calculated yield strength ($\sigma_{calculated}$) was obtained as the sum of the σ_0 , σ_{Taylor} and σ_{HP} , while the estimated values ($\sigma_{estimated}$) were determined as one-third of the hardness. The corresponding shear strain values calculated from eq. (1) are also shown. The calculation details of the shear strain are given in section 4.3.

Location	γ	σ ₀ [MPa]	σ_{Taylor} [MPa]	σ _{HP} [MPa]	σ _{calculated} [MPa]	$\sigma_{estimated}$ [MPa]
1/4 turn, center	1.1	879	131 ± 11	8 ± 1	1018 ± 81	944 ± 47
1/4 turn, periphery	9.1	879	247 ± 20	86 ± 7	1212 ± 97	1167 ± 58
1 turn, center	4.5	879	254 ± 20	11 ± 1	1144 ± 91	1038 ± 52
1 turn, periphery	36	879	303 ± 24	138 ± 11	1320 ± 106	1298 ± 65
10 turns, center	46	879	302 ± 24	128 ± 10	1309 ± 105	1180 ± 59
10 turns, periphery	369	879	304 ± 24	159 ± 13	1342 ± 107	1463 ± 73
20 turns, center	87	879	305 ± 24	137 ± 11	1321 ± 106	1302 ± 65
20 turns, periphery	698	879	307 ± 24	167 ± 13	1353 ± 108	1429 ± 72

- ~2600 MPa to ~3800 MPa in the early stage of deformation up to shear strain of 40. The hardness value was further enhanced to the maximum 4450 MPa owing to the grain refinement where the hardness of the HfNbTiZr HEA processed by HPT show reasonably similar hardness reported for the five-component counterparts.
- 3. A comparison between the calculated and the experimentally estimated yield strength values revealed that most hardening (60–90%) is introduced by the friction stress. This value is much higher than that obtained previously for fcc HEAs processed by HPT (10–20%). The dislocation strengthening shows higher contribution with more than a factor of two than the grain refinement strengthening to the total strength. On the other hand, the grain size hardening tends to be important for the total strength in the shear strain range of ~40 and ~400.

Acknowledgement

This work was supported in part by the Ministry of Human Capacities of Hungary within the ELTE University Excellence program (1783-3/2018/FEKUTSRAT); in part by the grant no. VEKOP-2.3.3-15-2016-00002 of the European Structural and Investment Funds; and in part by the National Science Foundation (United States) under Grant No. DMR-1810343. The authors are grateful to Dr. Károly Havancsák for the surface preparation for the EBSD investigations and Mr. Zsolt Maksa for the EBSD experiments. The preparation of the TEM lamellae by Andrea Fenyvesi-Jakab is also acknowledged.

Appendix A. Supplementary data

Supplementary data to this article can be found online at https://doi.org/10.1016/j.jallcom.2019.02.220.

References

- J.W. Yeh, S.-K. Chen, S.-J. Lin, J.-Y. Gan, T.-S. Chin, T.-T. Shun, C.-H. Tsau, S.-Y. Chang, Nanostructured high-entropy alloys with multiple principal elements: novel alloy design concepts and outcomes, Adv. Eng. Mater. 6 (2004) 299–303.
- [2] B. Cantor, I.T.H. Chang, P. Knight, A.J.B. Vincent, Microstructural development in equiatomic multicomponent alloys, Mater. Sci. Eng. A 375–377 (2004) 213–218.
- [3] D.B. Miracle, J.D. Miller, O.N. Senkov, C. Woodward, M.D. Uchic, J. Tiley, Exploration and development of high entropy alloys for structural applications, Entropy 16 (2014) 494–525.
- [4] Y. Zou, H. Ma, R. Spolenak, Ultrastrong ductile and stable high-entropy alloys at small scales. Nat. Commun. 6 (2015) 1—8.
- [5] Y. Zhang, T.T. Zuo, Z. Tang, M.C. Gao, K.A. Dahmen, P.K. Liaw, Z.P. Lu, Microstructures and properties of high-entropy alloys, Prog. Mater. Sci. 61 (2014) 1–93
- [6] O.N. Senkov, J.M. Scott, S.V. Senkova, F. Meisenkothen, D.B. Miracle, C.F. Woodward, Microstructure and elevated temperature properties of a refractory TaNbHfZrTi alloy, J. Mater. Sci. 47 (2012) 4062–4074.
- [7] S. Praveen, J.W. Bae, P. Asghari-Rad, J.M. Park, H.S. Kim, Ultra-high tensile strength nanocrystalline CoCrNi equi-atomic medium entropy alloy processed by high-pressure torsion, Mater. Sci. Eng. A 735 (2018) 394–397.
 [8] A. Gali, E.P. George, Tensile properties of high- and medium-entropy alloys,
- [8] A. Gali, E.P. George, Tensile properties of high- and medium-entropy alloys Intermetallics 39 (2013) 74–78.
- [9] Z. Wu, H. Bei, G.M. Pharr, E.P. George, Temperature dependence of the mechanical properties of equiatomic solid solution alloys with face-centered cubic crystal structures, Acta Mater. 81 (2014) 428–441.
- [10] G. Laplanche, A. Kostka, C. Reinhart, J. Hunfeld, G. Eggeler, E.P. George, Reasons for the superior mechanical properties of medium-entropy CrCoNi compared to high-entropy CrMnFeCoNi, Acta Mater. 128 (2017) 292–303.
- [11] Q. Lin, J. Liu, X. An, H. Wang, Y. Zhang, X. Liao, Cryogenic-deformation-induced phase transformation in an FeCoCrNi high-entropy alloy, Mater. Res. Lett. 6 (2018) 236–243.
- [12] J. Gubicza, M. El-Tahawy, Y. Huang, H. Choi, H. Choe, J.L. Lábár, T.G. Langdon, Microstructure, phase composition and hardness evolution in 316L stainless steel processed by high-pressure torsion, Mater. Sci. Eng. A 657 (2016) 215–223
- [13] Q.H. Tang, Y. Huang, Y.Y. Huang, X.Z. Liao, T.G. Langdon, P.Q. Dai, Hardening of an Al0.3CoCrFeNi high entropy alloy via high-pressure torsion and thermal

- annealing, Mater. Lett. 151 (2015) 126-129.
- [14] R. Zheng, J. Chen, W. Xiao, C. Ma, Microstructure and tensile properties of nanocrystalline (FeNiCoCu)1-xTixAlx high entropy alloys processed by high pressure torsion. Intermetallics 74 (2016) 38–45.
- [15] P.F. Yu, H. Cheng, L.J. Zhang, H. Zhang, Q. Jing, M.Z. Ma, P.K. Liaw, G. Li, R.P. Liu, Effects of high pressure torsion on microstructures and properties of an Al0.1CoCrFeNi high-entropy alloy, Mater. Sci. Eng. A 655 (2016) 283–291.
- [16] W. Wu, M. Song, S. Ni, J. Wang, Y. Liu, B. Liu, X. Liao, Dual mechanisms of grain refinement in a FeCoCrNi high entropy alloy processed by high pressure torsion, Sci. Rep. 7 (2017) 46720.
- [17] A. Heczel, M. Kawasaki, J.L. Lábár, J. il Jang, T.G. Langdon, J. Gubicza, Defect structure and hardness in nanocrystalline CoCrFeMnNi high-entropy alloy processed by high-pressure torsion, J. Alloys Compd. 711 (2017) 143—154.
- [18] A. Heczel, Y. Huang, T.G. Langdon, J. Gubicza, Investigation of lattice defects in a plastically deformed high-entropy alloy, Mater. Sci. Forum 885 (2017) 74–79.
- [19] H. Shahmir, M. Nili-Ahmadabadi, A. Shafiee, T.G. Langdon, Hardening and thermal stability of a nanocrystalline CoCrFeNiMnTi0.1 high-entropy alloy processed by high pressure torsion, IOP Conf. Ser. Mater. Sci. Eng. 194 (2017), 012017.
- [20] T.S. Reddy, I.S. Wani, T. Bhattacharjee, S.R. Reddy, R. Saha, P.P. Bhattacharjee, Severe plastic deformation driven nanostructure and phase evolution in a Al0.5CoCrFeMnNi dual phase high entropy alloy, Intermetallics 91 (2017) 150–157.
- [21] J. Moon, Y. Qi, E. Tabachnikova, Y. Estrin, W.-M. Choi, S.-H. Joo, B.-J. Lee, A. Podolskiy, M. Tikhonovsky, H.S. Kim, Microstructure and mechanical properties of high-entropy alloy Co20Cr26Fe20Mn20Ni14 processed by highpressure torsion at 77 K and 300 K, Sci. Rep. 8 (2018) 11074.
- [22] H. Shahmir, M. Nili-Ahmadabadi, A. Shafiee, M. Andrzejczuk, M. Lewandowska, T.G. Langdon, Effect of Ti on phase stability and strengthening mechanisms of a nanocrystalline CoCrFeMnNi high-entropy alloy, Mater. Sci. Eng. A 725 (2018) 196–206.
- [23] N.D. Stepanova, N.Yu. Yurchenko, A.O. Gridneva, S.V. Zherebtsov, YuV. Ivanisenko, G.A. Salishchev, Structure and hardness of B2 ordered refractory AlNbTiVZr0.5 high entropy alloy after high-pressure torsion, Mater. Sci. Eng. A 716 (2018) 308–315.
- [24] J. Qiang, K. Tsuchiya, H. Diao, P.K. Liaw, Vanishing of room-temperature slip avalanches in a face-centered-cubic high-entropy alloy by ultrafine grain formation, Scripta Mater. 155 (2018) 99–103.
- [25] H. Shahmira, M. Nili-Ahmadabadia, A. Shafieea, T.G. Langdon, Effect of a minor titanium addition on the superplastic properties of a CoCrFeNiMn highentropy alloy processed by high-pressure torsion, Mater. Sci. Eng. A 718 (2018) 468–476.
- [26] J. Cízek, P. Hausild, M. Cieslar, O. Melikhova, T. Vlasak, M. Janecek, R. Kral, P. Harcuba, F. Lukac, J. Zýka, J. Malek, J. Moon, H.S. Kim, Strength enhancement of high entropy alloy HfNbTaTiZr by severe plastic deformation, J. Alloys Compd. 768 (2018) 924–937.
- [27] B. Schuh, B. Volker, J. Todt, N. Schell, L. Perriere, J. Li, J.P. Couzinie, A. Hohenwarter, Thermodynamic instability of a nanocrystalline, single-phase TiZrNbHfTa alloy and its impact on the mechanical properties, Acta Mater. 142 (2018) 201–212.
- [28] S. Zherebtsov, N. Stepanov, Y. Ivanisenko, D. Shaysultanov, N. Yurchenko, M. Klimova, G. Salishchev, Evolution of microstructure and mechanical properties of a CoCrFeMnNi high-entropy alloy during high-pressure torsion at room and cryogenic temperatures, Metals 8 (2018) 123.
- [29] Y.D. Wu, Y.H. Cai, T. Wang, J.J. Si, J. Zhu, Y.D. Wang, X.D. Hui, A refractory Hf25Nb25Ti25Zr25 high-entropy alloy with excellent structural stability and tensile properties, Mater. Lett. 130 (2014) 277–280.
- [30] R.B. Figueiredo, P.R. Cetlin, T.G. Langdon, Using finite element modeling to examine the flow processes in quasi-constrained high-pressure torsion, Mater. Sci. Eng. A 528 (2011) 8198–8204.
- [31] D.P. Nelson, J.B. Riley, An experimental investigation of extrapolation methods in the derivation of accurate unit-cell dimensions of crystals, Proc. Phys. Soc. 57 (1945) 160–177.
- [32] G. Řibárik, J. Gubicza, T. Ungár, Correlation between strength and microstructure of ball-milled Al-Mg alloys determined by X-ray diffraction, Mater. Sci. Eng. A 387–389 (2004) 343–347.
- [33] L. Vitos, Computational Quantum Mechanics for Materials Engineers: the EMTO Method and Applications, Springer-Verlag, London, 2007.
- [34] A.P. Zhilyaev, T.G. Langdon, Using high-pressure torsion for metal processing: fundamentals and applications, Prog. Mater. Sci. 53 (2008) 893–979.
- [35] Y. Estrin, A. Molotnikov, D.H.J. Davies, R. Lapovok, Strain gradient plasticity modelling of high-pressure torsion, J. Mech. Phys. Solid. 56 (2008) 1186–1202
- [36] K. Edalati, T. Fujioka, Z. Horita, Evolution of mechanical properties and microstructures with equivalent strain in pure Fe processed by high pressure torsion, Mater. Trans. 50 (2009) 44–50.
- [37] A. Vorhauer, R. Pippan, On the homogeneity of deformation by high pressure torsion, Scripta Mater. 51 (2004) 921–925.
- [38] S. Sabbaghianrad, J. Wongsa-Ngam, M. Kawasaki, T.G. Langdon, An examination of the saturation microstructures achieved in ultrafine-grained metals processed by high-pressure torsion, J. Mater. Res. Technol. 3 (2014) 319–326.
- [39] S.A. Alsubaie, P. Bazarnik, M. Lewandowska, Y. Huang, T.G. Langdon, Evolution of microstructure and hardness in an AZ80 magnesium alloy processed by high-pressure torsion, J. Mater. Res. Technol. 5 (2016) 152–158.

- [40] J. Cízek, M. Janecek, T. Krajnák, J. Stráská, P. Hruska, J. Gubicza, H.S. Kim, Structural characterization of ultrafine-grained interstitial-free steel prepared by severe plastic deformation, Acta Mater. 105 (2016) 258–272.
- [41] G.M. Pharr, E.G. Herbert, Y. Gao, The indentation size effect: a critical examination of experimental observations and mechanistic interpretations, Annu. Rev. Mater. Res. 40 (2010) 271–292.
- [42] G. Dirras, J. Gubicza, A. Heczel, L. Lilenstein, J.-P. Couzinié, L. Perrière, Y. Guillot, A. Hocini, Microstructural investigation of plastically deformed Ti20Zr20Hf20Nb20Ta20 high entropy alloy by X-ray diffraction and transmission electron microscopy, Mater. Char. 108 (2015) 1–7.
- [43] D. Tabor, The hardness and strength of metals, J. Inst. Met. 79 (1951) 1–18.
- [44] G.I. Taylor, Plastic strain in metals, J. Inst. Met. 62 (1938) 307–324.
- [45] E.O. Hall, The deformation and ageing of mild steel: discussion of results, Proc. Phys. Soc. Lond. B 64 (1951) 747–753.
- [46] N.J. Petch, The cleavage strength of polycrystals, J. Iron Steel Inst. 173 (1953) 25-28.
- [47] Q. Li, Modeling the microstructure-mechanical property relationship for a 12CT-2W-V-Mo-Ni power plant steel, Mater. Sci. Eng. 361 (2003) 385–391.
- [48] R. Madec, L.P. Kubin, Second-order junctions and strain hardening in bcc and fcc crystals, Scr. Mater. 58 (2008) 767-770.

- [49] P.L. Mosbrucker, D.W. Brown, O. Anderoglu, L. Balogh, S.A. Maloy, T.A. Sisneros, J. Almer, E.F. Tulk, W. Morgenroth, A.C. Dippel, Neutron and Xray diffraction analysis of the effect of irradiation dose and temperature on microstructure of irradiated HT-9 steel, J. Nucl. Mater. 443 (2013) 522–530.
- [50] J.B. Jeon, B.-J. Lee, Y.W. Chang, Molecular dynamics simulation study of the effect of grain size on the deformation behavior of nanocrystalline bodycentered cubic iron, Scripta Mater. 64 (2001) 494–497.

 [51] J. Gubicza, Defect Structure and Properties of Nanomaterials, Woodhead
- Publishing, Duxford, UK, 2017.
- [52] W.H. Liu, Y. Wu, J.Y. He, T.G. Nieh, Z.P. Lu, Grain growth and the Hall—Petch relationship in a high-entropy FeCrNiCoMn alloy, Scripta Mater. 68 (2013) 526-529.
- [53] D.H. Lee, I.C. Choi, M.Y. Seok, J. He, Z. Lu, J.Y. Suh, M. Kawasaki, T.G. Langdon, J. il Jang, Nanomechanical behavior and structural stability of a nanocrystalline CoCrFeNiMn high-entropy alloy processed by high-pressure torsion, I. Mater. Res. 30 (2015) 2804–2815.
- [54] D.H. Lee, J.M. Park, G. Yang, J. He, Z. Lu, J.Y. Suh, M. Kawasaki, U. Ramamurty, J. il Jang, Nano-graining a particle-strengthened high-entropy alloy, Scripta Mater. 163 (2019) 24–28.